applied sciences

MDPI

Article

Grain Size Effects in Selective Laser Melted Fe-Co-2V

Wesley Everhart [1,*] and Joseph Newkirk [2]

[1] Honeywell Federal Manufacturing & Technologies LLC, Kansas City National Security Campus, Kansas City, MO 64147, USA
[2] Materials Science & Engineering, Missouri University of Science and Technology, Rolla, MO 65409, USA
* Correspondence: weverhart@kcnsc.doe.gov

Received: 1 August 2019; Accepted: 23 August 2019; Published: 6 September 2019

Abstract: The material science of additive manufacturing (AM) has become a significant topic due to the unique way in which the material and geometry are created simultaneously. Major areas of research within inorganic materials include traditional structural materials, shape memory alloys, amorphous materials, and some new work in intermetallics. The unique thermal profiles created during selective laser melting (SLM) may provide new opportunities for processing intermetallics to improve mechanical and magnetic performance. A parameter set for the production of Fe-Co-2V material with additive manufacturing is developed and efforts are made to compare the traditional wrought alloy to the AM version of the same chemistry. Evaluation includes magnetic properties, composition, and phase as a function of thermal history, as well as mechanical performance. Results show significant similarities in microstructure between AM and wrought materials, as well as mechanical and magnetic performance. Property trends are evaluated as a function of grain size and show effects similar to the Hall–Petch strengthening observed in wrought material, though with some underprediction of the strength. Magnetic properties qualitatively follow the expected trends but demonstrate some deviation from wrought material, which is still unexplained.

Keywords: additive manufacturing; magnetic materials; grain size effects

1. Introduction

With advances in the additive manufacturing (AM) of inorganic materials, a variety of efforts to understand the effects of this unique process on structure and properties have been undertaken. Such efforts have led many to question the use of materials designed for traditional wrought processes in AM and research has evolved to study the effects of AM processing on more unusual materials such as intermetallics. Specific work in intermetallics has been focused on materials such as titanium aluminides for high temperature strength, oxidation resistance, and creep resistance in the aerospace industry [1–4], or nickel titanium intermetallics for shape memory, damping, and biocompatibility for implants in the medical industry [5–9]. Only a few publications have investigated the potential for the selective laser melting (SLM) of magnetic intermetallics [10–13].

Mikler et al. [10] investigated the directed energy deposition (DED) of Ni-Fe-V and Ni-Fe-Mo soft magnets from an elemental powder blend. They found these materials exhibited similar saturation limits to traditional materials of similar chemistry, but with much higher coercivity. The difference in coercivity was attributed to microstructural defects such as porosity, unmelted particles, and other impurities, while grain size effects were not considered.

Schonrath et al. [11] produced Fe-Ni soft magnets from elemental powders using DED. This work showed incomplete homogenization with chemical segregation along weld boundaries, which was associated with increases in magnetic anisotropy. The AM material also showed a higher magnetic saturation than the elemental powder mixture, but this is likely due to the differences in phases present

in pure Fe or Ni as opposed to the intermetallic $FeNi_3$ since traditionally manufactured $FeNi_3$ has higher saturation than the AM material produced here. Evaluation of magnetics in various orientations relative to the AM process showed no anisotropy in the results.

Garibaldi et al. [12] produced Fe-6Si using SLM. They demonstrated the effects of altered build parameters and heat treatments on magnetic properties and hardness. Higher laser energies tend to drive toward a more highly textured material, which was shown to drive variation in magnetic properties. These changes are associated with the preferred magnetization direction of the crystal structure and its relation to the manufactured texture. Additionally, small grain size from the AM process was identified as a potential cause of reduced magnetic performance.

Kustas et al. [13] developed DED parameters for Fe-Co-1.5V and evaluated mechanical and magnetic properties related to structure in the as-built and ordered states. Results showed a near-random texture in the as-built state with a grain size on the order of 2.0 µm. The small grain size is attributed to a layer-by-layer reheating from the DED process. After annealing, a bimodal grain distribution was observed with the formation of 200–600-µm grains surrounded by the smaller grains remaining from the AM process. This abnormal grain growth may be caused by grain pinning of second phases such as oxides or the common $(Co,Fe)_3V$ precipitate. Magnetic properties in the as-built condition were shown to exhibit a higher level of coercivity with more sheared hysteresis loops, while annealed samples had lower coercivity and higher squareness.

This work intends to evaluate SLM Hiperco 50A (48.75 wt.% Co, 2.0 wt.% V, remainder Fe) structures and their relationship to mechanical and magnetic properties. This will be done through comparison with accepted relationships for wrought Hiperco 50A. Connections between grain size and mechanical and magnetic properties are explored and deviations of AM material from expected trends are highlighted.

2. Materials and Methods

The starting materials for this research, Hiperco 50A 1.0-inch diameter bar stock and Hiperco 50A powder specified to a 15–45 µm normal size distribution were both procured from Carpenter Technology Corporation (Philidelhpia, PA, USA). Powder was observed to be generally spherical and flowed sufficiently in the AM process to avoid any recoating defects. AM parameters (Table 1) were developed for Hiperco 50A powder on an EOS M 100 system (Krailling, Germany) with a 35-µm diameter laser.

Table 1. Additive manufacturing (AM) processing parameters for EOS M100.

Power (W)	Velocity (mm/s)	Hatch Spacing (mm)	Layer Thickness (mm)
110	880	0.05	0.02

AM and wrought samples were subjected to two main heat treatments. The first heat treatment heated up to the gamma phase field and was subsequently quenched in order to generate a structure with a high ductility, which is typically used for the rolling of wrought material. The second treatment was an ordering treatment that is required to obtain high magnetic saturation. Both heat treatment schedules are shown in Figure 1 and were performed in an inert gas furnace under 99.997% purity argon. Any oxidation from the heat treatments was removed with an abrasive prior to testing. Samples from the AM process with no heat treatment were also prepared for comparison.

Samples in each condition were tested for density, chemistry, mechanical properties, and magnetic hysteresis. Results were evaluated for trends between the microstructure and the mechanical and magnetic performance. Grain size measurement was performed on optical microstructures using the intercept method with 500 lines. Electron back scatter diffraction (EBSD) was performed on a subset of samples to confirm grain size measurements and evaluate potential texture. EBSD was completed on at least 400 grains with a 25-kV beam voltage and a 5-nA current. Chemistry was evaluated using acid digestion followed by inductively coupled plasma atomic emission spectrometry and inert gas

fusion per American Society for Testing and Materials (ASTM) E1019 [14]. Mechanical properties were evaluated as per ASTM E8 [15] on R4 samples under room temperature conditions with loading rates maintained below 0.00025 mm/(mm·s). Elongation to failure, ultimate tensile strength (UTS), and 0.2% offset yield strength (YS) were calculated from the results. Magnetic hysteresis was evaluated as per ASTM A773 [16] using ring samples for AM material and bar samples for wrought material.

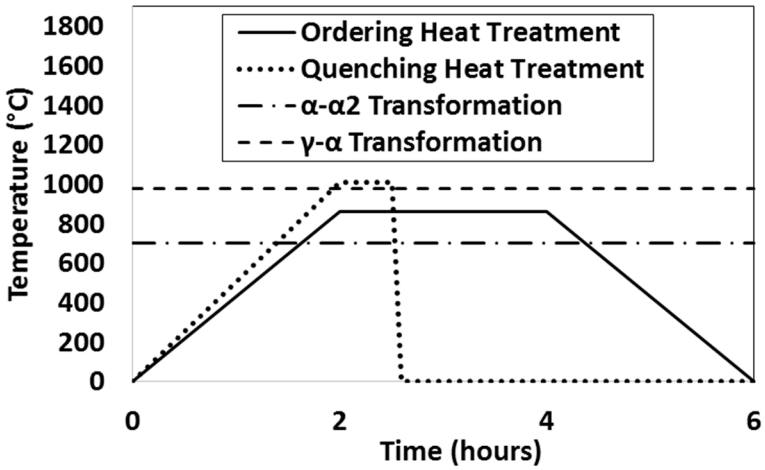

Figure 1. Ordering and quenching heat treatment schedules.

3. Results

The process parameters used (Table 1) resulted in high density (>99.9%) samples with no obvious cracking or porosity. Microstructures of each heat treatment condition are shown in Figure 2. It can be clearly seen that the as-built and quenched AM structures closely resembled the quenched wrought structure as each system had an irregular grain shape. In all heat treatment conditions, the AM samples had significantly smaller grain sizes than the wrought samples and irregularly shaped grains. The wrought material had equiaxed grains in the ordered condition and irregularly shaped grains in the quenched condition. Chemistry results are shown in Table 2 and show that the AM material had a much higher oxygen content and a slightly lower vanadium content compared to the wrought materials. The wrought material had 50.4 at.% iron and was therefore stoichiometrically lean in cobalt, while the AM material had 49.6 at.% iron and was therefore lean on both iron and cobalt, but only slightly so for iron.

Table 2. Nominal composition of Hiperco 50A and measured chemistry with test precision for wrought and AM material.

Element	Nominal (wt.%) [17]	Wrought (wt.%)	AM (wt.%)
Carbon	0.00	<0.001 ± 0.0003	<0.001 ± 0.0003
Manganese	0.05	0.029 ± 0.0040	0.026 ± 0.0040
Silicon	0.05	0.040 ± 0.0004	0.042 ± 0.0004
Cobalt	48.75	48.706 ± 0.0733	49.809 ± 0.0733
Vanadium	2.00	1.996 ± 0.0046	1.720 ± 0.0046
Oxygen	-	0.016 ± 0.0001	0.047 ± 0.0001
Iron	49.15	49.213 ± 0.0729	48.356 ± 0.0729

EBSD evaluation of ordered wrought material (Figure 3a) showed equiaxed grain morphology with a grain size of 49.32 ± 6.69 µm and minimal texture or misorientation. AM material showed a significantly smaller grain size of 5.87 ± 0.38 µm and a distorted microstructure with elongated and

curved grains (Figure 3b,c). Regions of grain growth and altered grain morphology were observed in the AM material after 2 h of ordering (Figure 3b).

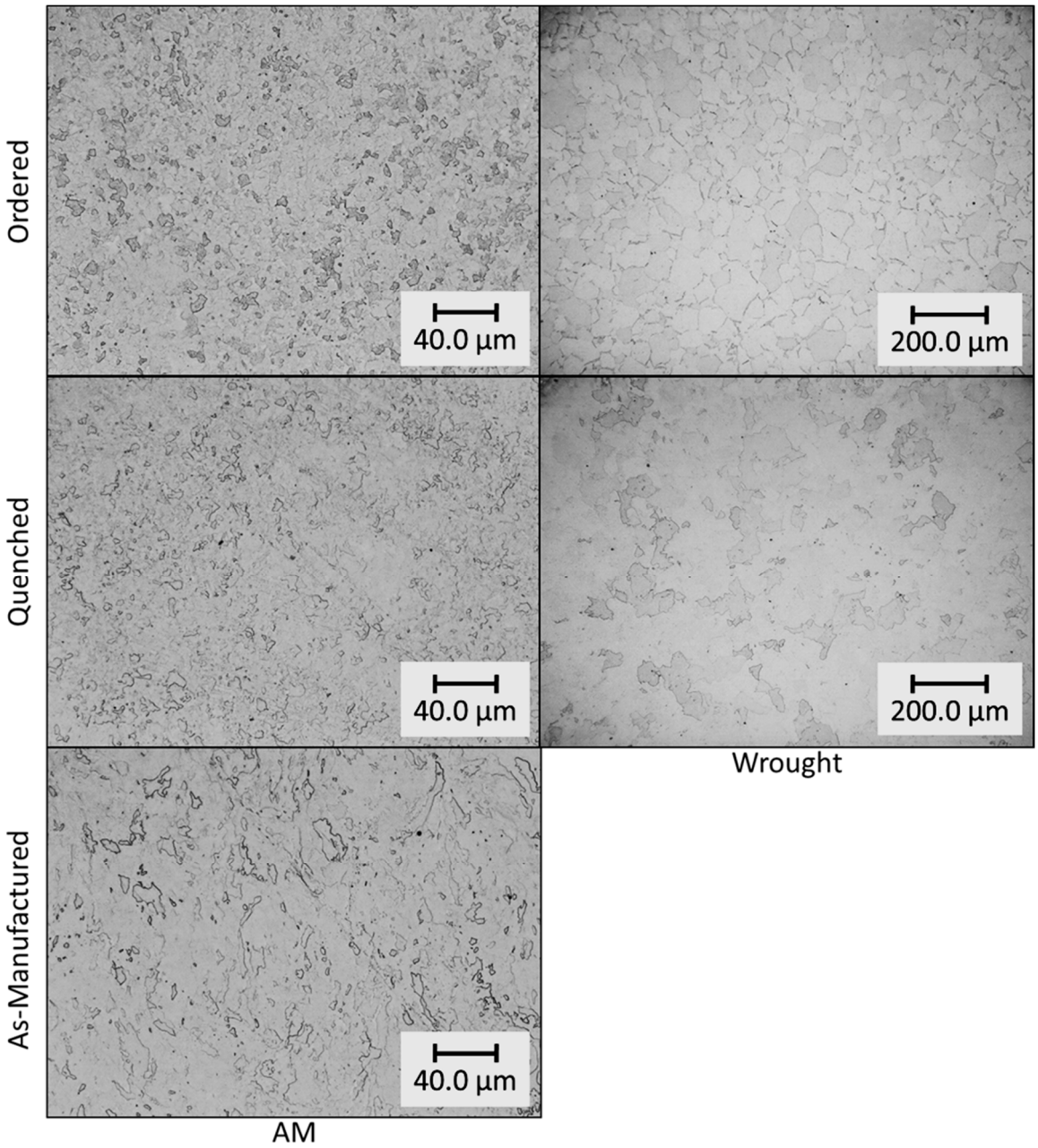

Figure 2. Characteristic microstructures of AM and wrought material in various heat treatment conditions. AM images are on the left and wrought images are on the right. Samples were etched with Ralph's reagent.

Tensile test curves for each heat treatment condition can be seen in Figure 4. Figure 4a shows the engineering stress–strain curves for quenched and as-built AM samples, which all showed high levels of ductility. The wrought material showed the lowest strength, followed by quenched AM material and then the as-built AM material. Each material had similar ductility; however, the as-built AM sample showed greater variation in ductility as well as the lower average values. Figure 4b shows the stress–strain curves for the ordered condition for both AM and wrought materials. Both materials showed significantly lower ductility (<4%) than other conditions, with the AM material showing

significantly higher strength. The AM material also exhibited a significant secondary yield point behavior while the wrought material did not.

Figure 5 shows the two AM fracture morphologies observed in testing and is representative of the fracture morphologies observed in the wrought material. Microvoid coalescence was observed in the as-built and quenched AM material, as well as the quenched wrought material, indicating ductile rupture, while transgranular cleavage was observed for both materials in the ordered condition. Figure 6 shows the magnetic performance of AM material for various heat treatment conditions. The AM material underperformed in both the as-built condition and the quenched condition, with the quenched condition having the lower magnetic properties. Ordering the AM material improved the magnetic performance significantly, resulting in a more square-shaped hysteresis loop.

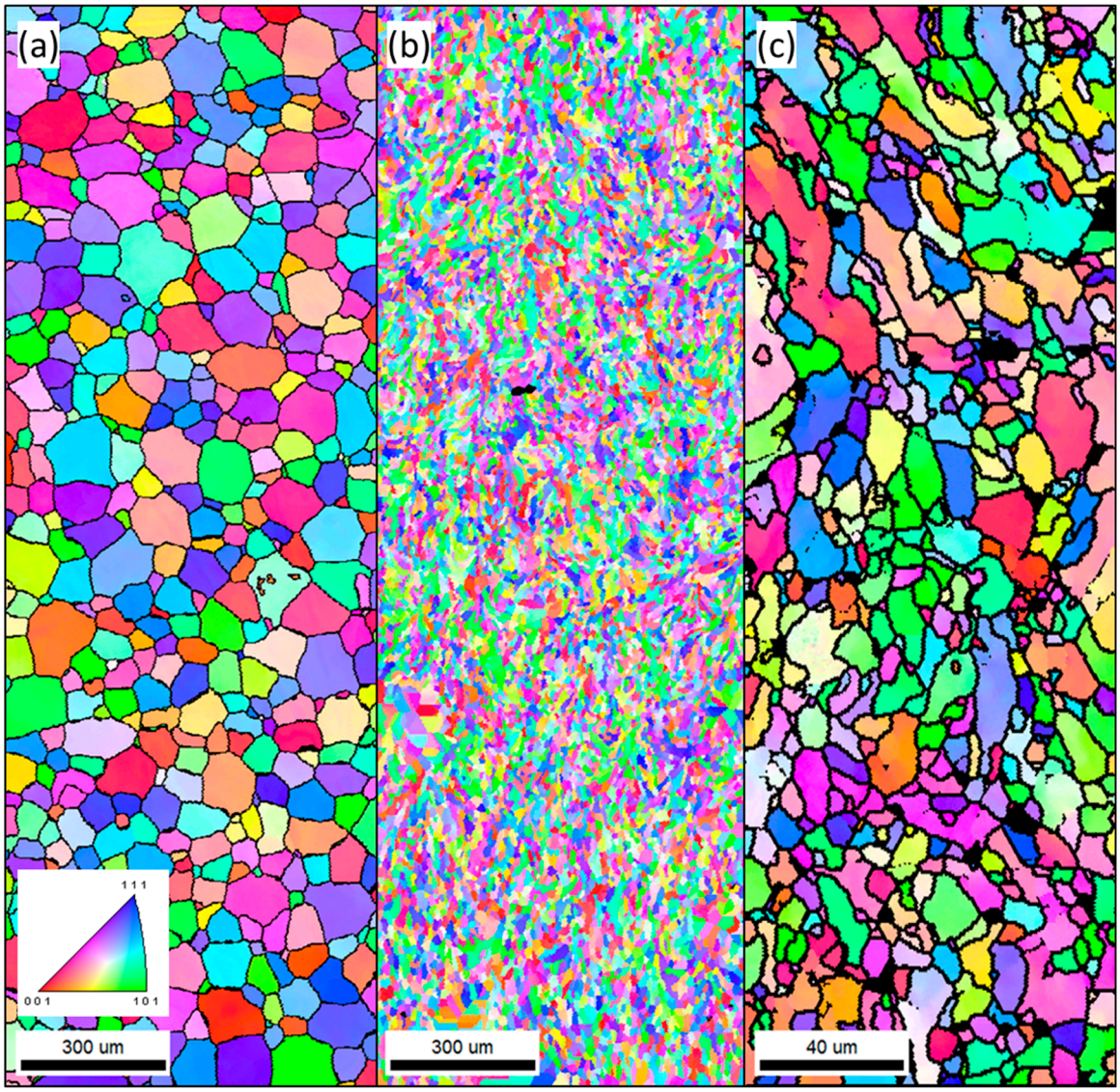

Figure 3. Electron back scatter diffraction (EBSD) crystal orientation images for ordered wrought material (**a**) and ordered AM material (**b**,**c**).

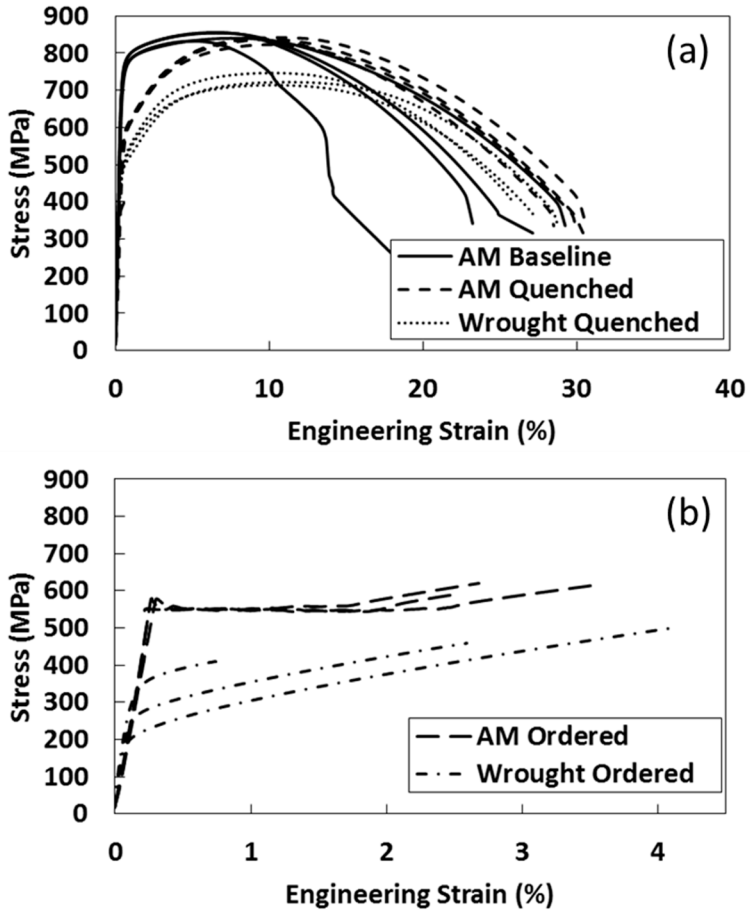

Figure 4. Representative stress–strain curves for high ductility conditions (**a**) and low ductility conditions (**b**).

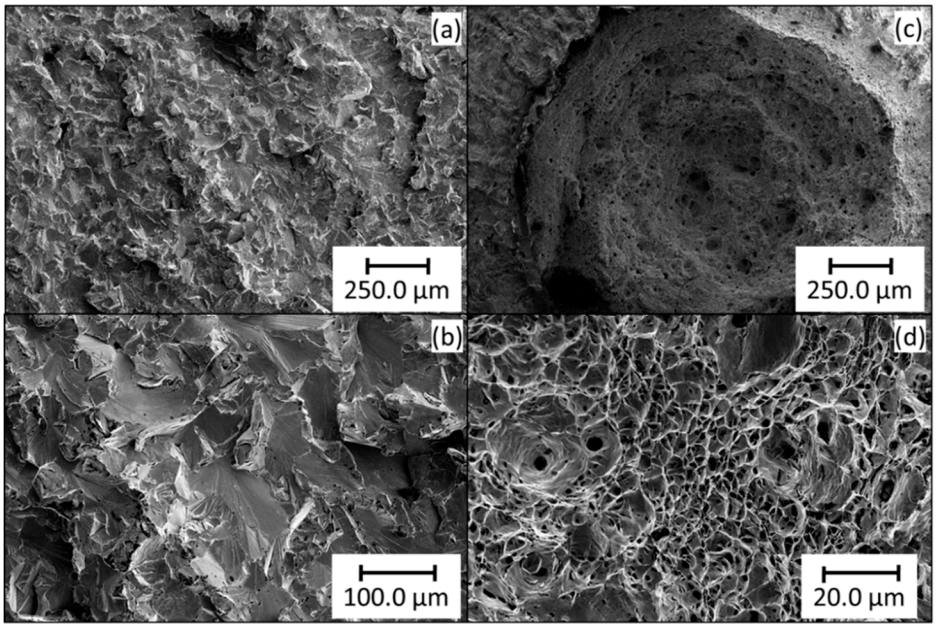

Figure 5. Fractographs of AM Hiperco in the ordered (**a**,**b**) and quenched (**c**,**d**) conditions.

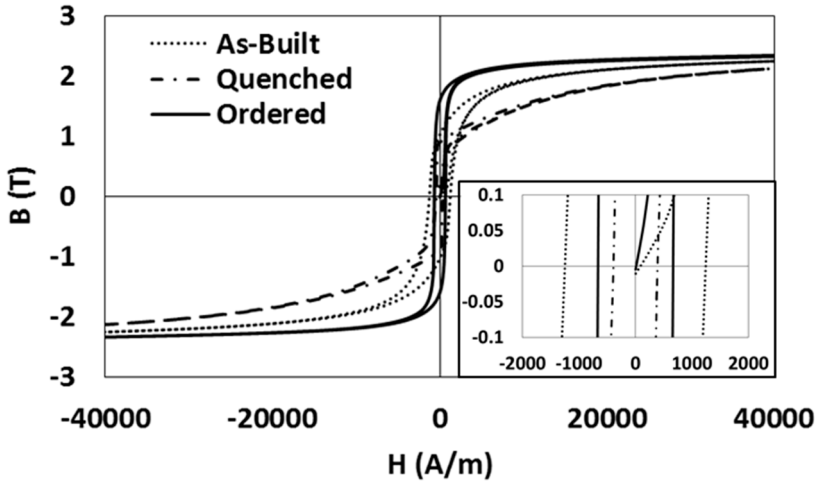

Figure 6. Representative hysteresis loops for AM samples for various heat treatment conditions. The inset figure illustrates the differences in coercivity.

4. Discussion

The as-built and quenched conditions of the AM material both showed high levels of ductility, low magnetic saturation, and a ductile fracture mode, which were all consistent with the structure and properties typically observed in quenched wrought material. This similarity between the as-built and quenched AM materials can be rationalized due to the observed high cooling rates in the AM process, which imparted a similar microstructure compared to a quenching treatment. It can be seen in Figure 2 that all the materials tested were fully dense and the porosity commonly found in AM materials was not expected to have significantly influenced properties. It still is not clear why the fast cooling rate drove the high ductility in traditional Fe-Co-V alloys, but the two major theories are the prevention of the ordering reaction or a martensitic transformation [18]. The largest observed difference between AM and wrought materials was the grain size, which was likely coupled with the observed yield strength difference. However, repeatable grain size measurements were not easily completed with these samples for the AM condition.

It has been previously shown that wrought Fe-Co alloys, such as Hiperco 50A, show a strong Hall–Petch relationship in the ordered condition [18]. Grain size measurements from this study for AM material ordered for 2 h revealed grain sizes of 5.87 ± 0.38 μm while wrought material in the same condition had grain sizes of 49.32 ± 6.69 μm. Figure 7 shows the common Hall–Petch relationship for Hiperco 50A from Sourmail [18], as well as the data from this study for both wrought and AM material aged for two hours. The wrought data clearly aligns well with the expected relationship; however, the AM data slightly overperformed the predicted strength for its grain size. While it is not clear what the specific driving force for this increased strength was, the higher oxygen content in the material, the smaller grain size, precipitate formation, and other possible non-standard microstructural features remnant from the AM process could be the cause and further work is needed to elucidate this behavior.

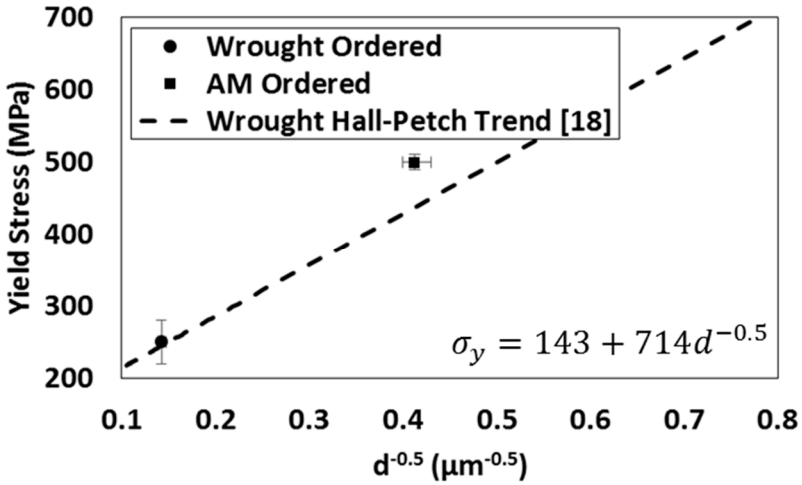

Figure 7. Hall-Petch fit of yield strength for both ordered AM and wrought material.

In addition to the deviation from the standard Hall–Petch relationship of the ordered AM material, the ordered AM material exhibited a strong yield point behavior, while the ordered wrought material did not. As discussed by Pitt and Rawlings [19], reduced grain sizes can increase the occurrence of Lüders strain behavior in Fe-Co alloys. The 1–2% strain of yield point behavior for ordered AM material matches closely to reported data for Lüders strain in wrought material with the same grain size, and the large grain size observed in the wrought samples has been shown to be sufficient to eliminate yield point behavior.

After the initial results of ordering treatment on the AM material exhibited high coercivity and insufficient saturation in low magnetic fields, a second ordering treatment was applied to both AM and wrought materials. A summary of results is shown in Figure 8. The most-square hysteresis curve was observed in the wrought material ordered for four hours, closely followed by the four-hour ordering of the AM material and the two-hour ordering for both materials. Similar to Hall–Petch behavior for yield strength, Fe-Co alloys exhibit an inverse relationship between grain size and coercivity, though this relationship has not been effectively explored for grain sizes below 5.0 μm [18]. Samples were re-evaluated for grain growth after the second ordering treatment. The wrought material showed almost no grain growth from the two additional hours of ordering with a final grain size of 51.48 ± 5.05 μm and the AM material showed significant grain growth with a final grain size of 8.91 ± 0.22 μm. As can be seen in Figure 9, all wrought and AM samples showed an unexpectedly high coercivity. When compared to commonly reported coercivity trends for wrought material, both the wrought and AM samples in this work, which were ordered for two hours, had similar deviations from the common trend line with an approximately 250 A/m higher coercivity than would be expected from their grain sizes. Wrought material that was exposed to a second ordering treatment showed a slight decrease in coercivity, which corresponded to the slight increase in grain size. These changes qualitatively matched the generally expected trend, though still did not align with previously reported values. The AM material exposed to a second ordering treatment showed an increase in coercivity that corresponded to the significant grain growth observed. This result is counter to the expected trend and could have several possible causes such as higher oxygen content, remnants of the AM solidification structure, or other sources of domain wall motion barriers.

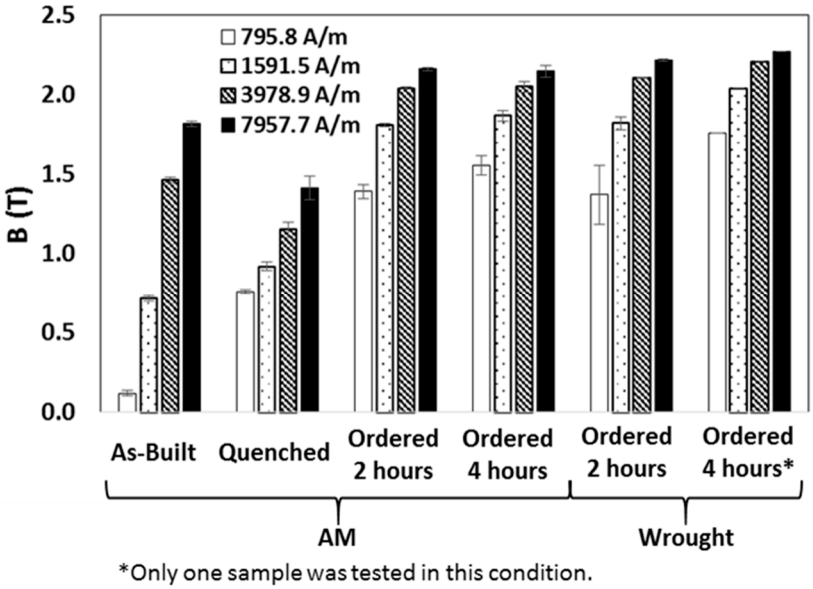

Figure 8. Magnetic saturation at various applied magnetic fields for AM and wrought samples.

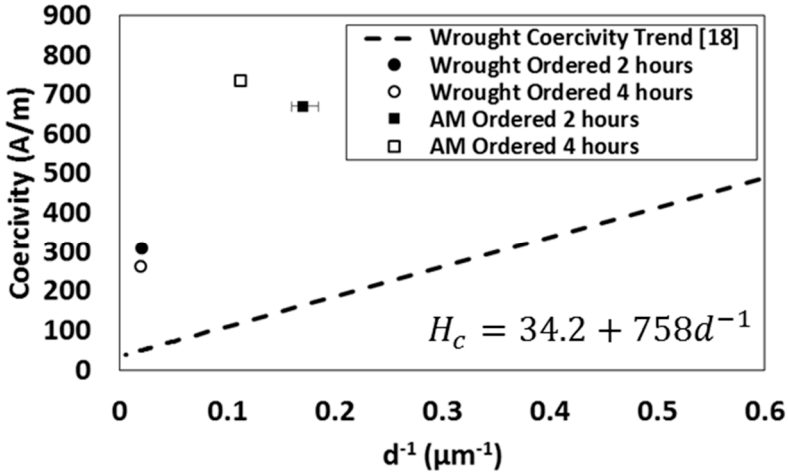

Figure 9. Coercivity data for wrought and AM materials after ordering for two or four hours compared to a previously reported grain size relationship for Fe-Co-2V.

In order to investigate the possibility of a second phase formation and its impact on the magnetic properties, XRD was performed on the samples using a Cu Kα source. Review of both AM and wrought material after four hours of ordering showed no significant presence of a second phase (Figure 10). Residual stress, texture, atypical grain boundary character, or nanometer-scale precipitates that might be present and might not be captured by XRD analysis are possible sources of the high coercivity. It is not expected that material aged at elevated temperature for 2–4 h and furnace -cooled would retain any significant residual stresses; however, it is possible that small stress gradients in the AM material could remain and contribute to the observed values. Transmission electron microscopy (TEM) could provide further insight into the structure of the material and its influence on coercivity, as well as identify any possible nanometer-scale precipitates. Such precipitates are commonly observed in AM microstructures and could be a source for both the slightly increased strength and higher coercivity observed in AM materials when compared to expected wrought material trends [20].

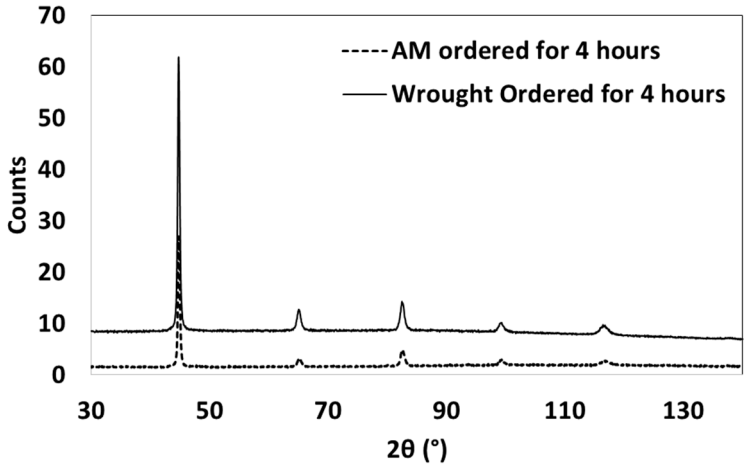

Figure 10. X-ray diffraction results for AM and wrought material ordered for four hours.

5. Conclusions

Bulk samples of Hiperco 50A were successfully manufactured using SLM and were evaluated for mechanical and magnetic properties in various heat treatment conditions. AM material was shown to behave similar mechanical manner to wrought material in the quenched condition and exhibited ductility in excess of 20% with lower magnetic saturation than the ordered condition. The as-built AM condition had a similar "quenched" structure and mechanical properties but had slightly better magnetic performance. The ordered material exhibited significant improvements to magnetic properties and expected levels of ductility and strength. Deviations of properties between the AM and wrought material were largely attributed to the Hall–Petch effect for yield strength, but coercivity of the AM material did not follow the expected trend with grain size. While additional work is necessary to understand the driving factors for these trends, SLM Hiperco 50A largely behaved the same as traditional wrought material. Further work is necessary to optimize heat treatment for magnetic performance, but it is likely that AM Hiperco 50A material can be effectively used in critical magnetic applications.

Author Contributions: Conceptualization, W.E. and J.N.; formal analysis, W.E. and J.N.; writing—original draft preparation, W.E.; writing—review and editing, J.N.

Funding: All data prepared, analyzed, and presented has been developed in a specific context of work and was prepared for internal evaluation and use pursuant to that work authorized under the referenced contract. Reference herein to any specific commercial product, process, or service by trade name, trademark, manufacturer, or otherwise, does not necessarily constitute or imply its endorsement, recommendation, or favoring by the United States Government, any agency thereof, or Honeywell Federal Manufacturing & Technologies, LLC. This presentation has been authored by Honeywell Federal Manufacturing & Technologies under Contract No. DE-NA0002839 with the U.S. Department of Energy.

Acknowledgments: The authors would like to thank David Wieliczka for EBSD analysis, Cory Read for XRD analysis, Phillip Hartman for metallography preparation, Ida Sanchez for help developing SLM parameter sets, and Ryan Zvanut, Samantha Tatar, Megan Bax, and Karen Bailey for help with material orders and testing.

Conflicts of Interest: The authors declare no conflict of interest.

References

1. Dilip, J.J.S.; Miyanaji, H.; Lassell, A.; Starr, T.L.; Stucker, B. A novel method to fabricate TiAl intermetallic alloy 3D parts using additive manufacturing. *Def. Technol.* **2017**, *13*, 72–76. [CrossRef]
2. Löber, L.; Schimansky, F.P.; Kühn, U.; Pyczak, F.; Eckert, J. Selective laser melting of a beta-solidifying TNM-B1 titanium aluminide alloy. *J. Mater. Process. Technol.* **2014**, *214*, 1852–1860. [CrossRef]
3. Tang, H.P.; Yang, G.Y.; Jia, W.P.; He, W.W.; Lu, S.L.; Qian, M. Additive manufacturing of a high niobium-containing titanium aluminide alloy by selective electron beam melting. *Mater. Sci. Eng. A* **2015**, *636*, 103–107. [CrossRef]

4. Grigoriev, A.; Polozov, I.; Sufiiarov, V.; Popovich, A. In-situ synthesis of Ti2AlNb-based intermetallic alloy by selective laser melting. *J. Alloys Compd.* **2017**, *704*, 434–442. [CrossRef]
5. Saedi, S.; Turabi, A.S.; Andani, M.T.; Haberland, C.; Karaca, H.; Elahinia, M. The influence of heat treatment on the thermomechanical response of Ni-rich NiTi alloys manufactured by selective laser melting. *J. Alloys Compd.* **2016**, *677*, 204–210. [CrossRef]
6. Saedi, S.; Turabi, A.S.; Andani, M.T.; Moghaddam, N.S.; Elahinia, M.; Karaca, H.E. Texture, aging, and superelasticity of selective laser melting fabricated Ni-rich NiTi alloys. *Mater. Sci. Eng. A* **2017**, *686*, 1–10. [CrossRef]
7. Bormann, T.; Schumacher, R.; Müller, B.; Mertmann, M.; de Wild, M. Tailoring Selective Laser Melting Process Parameters for NiTi Implants. *J. Mater. Eng. Perform.* **2012**, *21*, 2519–2524. [CrossRef]
8. Dadbakhsh, S.; Speirs, M.; Van Humbeeck, J.; Kruth, J.-P. Laser additive manufacturing of bulk and porous shape-memory NiTi alloys: From processes to potential biomedical applications. *MRS Bull.* **2016**, *41*, 765–774. [CrossRef]
9. Li, S.; Hassanin, H.; Attallah, M.M.; Adkins, N.J.E.; Essa, K. The development of TiNi-based negative Poisson's ratio structure using selective laser melting. *Acta Mater.* **2016**, *105*, 75–83. [CrossRef]
10. Mikler, C.V.; Chaudhary, V.; Borkar, T.; Soni, V.; Choudhuri, D.; Ramanujan, R.V.; Banerjee, R. Laser additive processing of Ni-Fe-V and Ni-Fe-Mo Permalloys: Microstructure and magnetic properties Ni-Fe-V. *Mater. Lett.* **2017**, *192*, 9–11. [CrossRef]
11. Schonrath, H.; Spasova, M.; Kilian, S.O.; Meckenstock, R.; Witt, G.; Sehrt, J.T.; Farle, M. Additive manufacturing of soft magnetic permalloy from Fe and Ni powders: Control of magnetic anisotropy. *J. Magn. Magn. Mater.* **2019**, *478*, 274–278. [CrossRef]
12. Garibaldi, M.; Ashcroft, I.; Hillier, N.; Harmon, S.A.C.; Hague, R. Relationship between laser energy input, microstructures and magnetic properties of selective laser melted Fe-6.9%wt Si soft magnets. *Mater. Charact.* **2018**, *143*, 144–151. [CrossRef]
13. Kustas, A.B.; Susan, D.F.; Johnson, K.L.; Whetten, S.R.; Rodriguez, M.A.; Dagel, D.J.; Michael, J.R.; Keicher, D.M.; Argibay, N. Characterization of the Fe-Co-1.5V soft ferromagnetic alloy processed by Laser Engineered Net Shaping (LENS). *Addit. Manuf.* **2018**, *21*, 41–52. [CrossRef]
14. ASTM International (ASTM). *ASTM Standard E1019, Standard Test Methods for Determination of Carbon, Sulfur, Nitrogen, and Oxygen in Steel, Iron, Nickel, and Cobalt Alloys by Various Combustion and Inert Gas Fusion Techniques*; ASTM International: West Conshohocken, PA, USA, 2018.
15. ASTM International (ASTM). *ASTM Standard E8, Standard Test Methods for Tension Testing of Metallic Materials*; ASTM International: West Conshohocken, PA, USA, 2015.
16. ASTM International (ASTM). *ASTM Standard A773, Standard Test Method for Direct Current Magnetic Properties of Low Coercivity Magnetic Materials Using Hysteresigraphs*; ASTM International: West Conshohocken, PA, USA, 2014.
17. Carpenter Technology Corporation. Carpenter CarTech ® Hiperco ® 50A Alloy. Available online: https://www.carpentertechnology.com/en/product-solutions/cartech-hiperco-50a-alloy/ (accessed on 1 January 2019).
18. Sourmail, T. Near equiatomic FeCo alloys: Constitution, mechanical and magnetic properties. *Prog. Mater. Sci.* **2005**, *50*, 816–880. [CrossRef]
19. Pitt, C.D.; Rawlings, R.D. Lüders strain and ductility of ordered Fe–Co–2V and Fe-Co-V-Ni alloys. *Met. Sci.* **1983**, *17*, 261–266. [CrossRef]
20. Wang, Y.M.; Voisin, T.; McKeown, J.T.; Ye, J.; Clata, N.P.; Li, Z.; Zeng, Z.; Zhang, Y.; Chen, W.; Roehling, T.T.; et al. Additively manufactured hierarchical stainless steels with high strength and ductility. *Nat. Mater.* **2018**, *17*, 63–71. [CrossRef] [PubMed]